

Direct measurement of optical properties of glacier ice using a photon-counting diffuse LiDAR

Markus ALLGAIER¹, Matthew G. COOPER², Anders E. CARLSON³, Sarah W. COOLEY⁴, Jonathan C. RYAN⁴, Brian J. SMITH¹

¹*Department of Physics and Oregon Center for Optical, Molecular, and Quantum Science, University of Oregon, Eugene, OR 97403, USA*

²*Pacific Northwest National Laboratory, Richland, WA 99354, USA*

³*Oregon Glacier Institute, Corvallis, OR 97330, USA*

⁴*Department of Geography, University of Oregon, Eugene, OR 97403, USA*

Correspondence: Markus Allgaier <markusa@uoregon.edu>

ABSTRACT. The interaction of light with glacier ice is governed by its optical scattering and absorption coefficients. These define apparent optical properties such as albedo and penetration depth of range finding lasers. Prior work has focused on snow or deep ice from cores rather than surface glacial ice. Consequently, the majority of measurements of the absorption coefficient of ice rely on assumptions about optical scattering and reference values derived from snow transmission measurements. Sophisticated physical albedo models only exist for snow, not for glacial surface ice. Here, we demonstrate a measurement technique based on diffuse propagation of nanosecond-duration laser pulses in glacier ice that enables the independent measurement of the scattering and absorption coefficients, allowing for a complete description of the processes governing radiative transfer. We employ a photon-counting detector to overcome the high losses associated with diffuse optics. The instrument is highly portable and rugged, making it optimally suited for deployment in remote regions. A set of measurements taken on Collier Glacier, Oregon, serves as a first demonstration of the technique. These measurements provide insight into both physical structure and composition of glacier ice and open new avenues for the analysis of light-absorbing impurities and remote sensing of the cryosphere.

INTRODUCTION

Mountain glaciers, ice caps, and ice sheets have been shrinking since the late 20th and early 21st century due to anthropogenic climate change and have contributed substantially to global sea-level rise (Meredith and others, 2019). Much of this glacier mass loss is due to warmer summer air temperatures, which initiate positive feedbacks between albedo and melt that further enhance mass loss. For example, warmer air temperatures increase snow grain sizes, causing more absorption of shortwave radiation and further melt (Gardner and Sharp, 2010). Other processes, particularly the deposition of light-absorbing particles (LAP) such as black carbon (BC) and dust are also known to reduce ice and snow albedo and enhance melt (Dumont and others, 2014; Skiles and others, 2018). More recently biological radiative forcing by algae has received much attention as a driver for enhanced snow and ice melt (Dial and others, 2018; Williamson and others, 2018; Ryan and others, 2018). Precise knowledge

of how glacial ice optical properties respond to warming air temperatures, BC, dust, and algae is therefore a prerequisite for accurately modeling glacier and ice sheet melt and subsequent contribution to sea levels.

Understanding the optical properties of glacial ice is not only important for modeling the radiative transfer and energy budgets of ice and snow, but also for remote sensing. Scattering of light within snow and glacial ice, for example, may introduce a bias in laser altimetry (Smith and others, 2018; Greeley and others, 2019). Photons that scatter multiple times below the surface take longer to return to the sensor, making the surface appear lower than it actually is. This process is especially important for the ATLAS instrument onboard ICESat-2, which operates at 532 nm, a wavelength known to have low absorption and strong forward scattering in snow and ice (Warren and Brandt, 2008). If not properly corrected, this process could introduce a centimeter to decimeter bias in sea ice, glacier and ice sheet elevations

derived from ICESat-2.

LAPs are of particular importance for albedo and subsequent melt rates of snow (Hadley and Kirchstetter, 2012; Kaspari and others, 2015; Zhang and others, 2017). There is a significant body of work dedicated to describing absorption, scattering, crystal structure, impurities and apparent optical properties of snow (Wiscombe and Warren, 1980; Warren and Wiscombe, 1980; Kokhanovsky and Zege, 2004; Libois and others, 2013; Saito and others, 2019; Beres and others, 2020). These models accurately reproduce field measurements of snow albedo. In contrast, relatively few studies have investigated the optical properties of glacial ice (see Warren and Brandt (2008) and Warren (2019) for comprehensive reviews). Perovich and Govoni (1991) derived absorption coefficients for pure bubble-free ice between 250–600 nm using a laboratory transmission measurements. Likewise, Ackermann and others (2006) derived scattering and absorption coefficients of glacier ice by measuring the frequency distribution of photon travel times from a pulsed light source in glacier ice deep in the Antarctic Ice Sheet as part of the Antarctic Muon and Neutrino Detector Array (AMANDA) experiment. However, the clean, bubble-free ice investigated by these studies is likely not representative of glacier ice exposed in the ablation zones of most ice masses.

So far, in-situ measurements of scattering and absorption coefficients of glacial ice have remained challenging. Transmission measurements rely on assumptions about the wavelength-independence of the scattering coefficient at visible wavelengths as well as the qualitative influence of LAPs, for which reference values are needed (Warren and others, 2006; Cooper and others, 2021). The same is true for scattering intensity measurements, where merely an effective constant describing both scattering and absorption can be retrieved (Allgaier and Smith, 2021). Although an attempt was made to retrieve independent values for scattering and absorption from experimentally measured scattering intensity distributions using numerical simulations (Trodahl and others, 1987), a truly independent measurement has only been shown in the framework of detector calibration for AMANDA and IceCube (Ackermann and others, 2006; Aartsen and others, 2013), where the propagation of short optical pulses through deep glacier ice at the South Pole was measured in the time domain. For this purpose, a diffusion transport model was developed (Askebjerg and others, 1997). However, this model was found to be inaccurate in bubble-free, deep ice, where the conditions to satisfy the diffusion approximation are not met due to insufficient scattering. Similar measurements performed on sea ice also cannot be described by the diffusion model since the detector is in the diffusion-near-field (Perron and others, 2021), close to the source. Because the

diffusion model has only two free parameters - effective scattering and absorption coefficients - it would be a convenient tool for measuring these properties on the surface of glaciers, sea ice and snow, where it would provide an independent measurement free of assumptions. Along with the refractive index, these two parameters are sufficient to calculate the albedo of glacial ice (Dombrovsky and Kokhanovsky, 2020). When albedo is inferred in this way, it can be interpreted in terms of scattering and absorption, which is not possible from albedo measurements alone. Numerical simulations have shown that the diffusion model is a robust tool to accomplish these measurements on the surface if the appropriate boundary conditions are considered (Allgaier and Smith, 2021).

Here, we present a new instrument that implements a time-resolved scattering experiment with a narrow-band point source on the surface. A photon-counting detector is placed in the scattering-far-field, several scattering lengths away from the source, which allows us to employ a diffusion model that includes appropriate boundary conditions to describe behavior at the surface, outlined in our recent theoretical analysis (Allgaier and Smith, 2021). The device is highly portable, making it ideal for deployment in rugged and remote areas. We show data measured in the field on Crook and Collier Glacier in the Central Oregon Cascades in September 2021. We conclude with a discussion about how data obtained with this instrument could inform surface energy balance models with accurate scattering and absorption coefficients, provide LiDAR and laser altimeter penetration depth, and provide a proxy for measuring BC concentration in glacier ice.

First, we provide a summary of the employed diffusion model and its implications on experimental resolution as well as context about the established terminology for scattering in glacier ice and snow. Next, we describe the instrument and its performance in terms of resolution and range. We present the experimental results of the measurements on Crook and Collier Glacier. Finally, we discuss statistical correlations of the data, compare extracted coefficients to the literature, and showcase how the measured scattering and absorption coefficients can be used to infer spectral and broadband albedo as well as LAP concentration.

DIFFUSE PROPAGATION OF A POINT SOURCE

Diffuse imaging has been employed in tissue for over two decades, where it is known that retrieval of both scattering and absorption parameters requires a modulated or non-stationary source in either spectrum or time (Durduran and

others, 2010). Transport of light in scattering media, particularly glacier ice, takes place on fairly long time scales. Therefore, implementation of diffuse measurements in the time-domain is convenient. Here, we restrict ourselves to geometries where source and detector are far apart. In the presence of both scattering and absorption, radiative transport in terms of a fluence rate $\phi(r, t)$, where r is the distance from the source and t is the time since injection of the instantaneous source, is described by the diffusion equation

$$\frac{\partial \phi(r, t)}{\partial t} = D \nabla^2 \phi(r, t) - c\beta\phi(r, t) + cS(r, t), \quad (1)$$

in which $c = c_0/n$ is the speed of light in the medium, c_0 is the vacuum speed of light, n is the refractive index and $S(R, T)$ is the source distribution. D is the diffusion constant, which is related to the effective, isotropic scattering constant:

$$D = \frac{cl_{\text{eff}}}{3} = \frac{c}{3\sigma_{\text{eff}}}. \quad (2)$$

Here, l_{eff} is the mean-free path of an effective, isotropic scattering process and the inverse scattering constant σ_{eff} . The well-known Green's function that solves this diffusion equation for an instantaneous point source at $r = 0, t = 0$ inside an infinite medium is

$$\phi_+(r, t) = \frac{1}{(4\pi Dt)^{3/2}} \exp\left(-\frac{r^2}{4Dt} - \beta t\right), \quad (3)$$

where $\beta = c/l_{\text{abs}} = c\sigma_{\text{abs}}$ dampens the flux at long times through absorption, described by the absorption length l_{abs} or absorption coefficient σ_{abs} . A detailed derivation of this solution and its relationship to a random walk in the photon picture can be found in Askebjerg and others (1997).

It is important to note that this description is only valid in the scattering-far-field, where $r \gg l_{\text{eff}}$, which practically means that a detector needs to be placed sufficiently far away from the source. To account for the fact that a realistic laser source is not isotropic, we replace it with an effective isotropic source that lies one scattering length below the surface. In reality, glacier ice is a compact medium with refractive index $n = 1.31$ (Warren, 2019), which means that a significant portion of the light impinging onto the surface from below is reflected back into the medium. To account for this, we adopt an appropriate boundary condition (Bryan, 1890; Haskell and others, 1994). Rigorous consideration of the Fresnel reflection at the surface and solving the corresponding boundary problem leads to a solution with three effective components: The effective source below the surface at $z = -l_{\text{eff}}$, another effective source at $z = l_{\text{eff}}$ above the surface, and a damped line of sinks:

$$\begin{aligned} \phi(\rho, t, z = 0) &= \phi_+(l_{\text{eff}}) + \phi_+(-l_{\text{eff}}) \\ &\quad - \frac{3(1-R)}{l_{\text{eff}}(1+R)} \int_0^\infty e^{-l/h} \phi_+(-l - l_{\text{eff}}) dl, \end{aligned} \quad (4)$$

with the average Fresnel reflection R as defined by Haskell and others (1994) and coordinates ρ, z as defined in Figure 1. A detailed derivation of this equation and its implication on retrieving scattering and absorption coefficient as well as volume depth can be found in Allgaier and Smith (2021). For an appropriate measurement, where a short pulse of light is injected into the medium at $\rho = 0, z = 0, t = 0$ and a detector is placed far away at ρ , this formula can be fitted to the measured fluence $\phi(\rho, t)$, with scattering coefficients σ_{eff} and absorption coefficient σ_{abs} (or the respective length scales $l_{\text{eff}}, l_{\text{abs}}$) as free parameters.

While this manuscript's focus is on measuring optical properties of bubbly glacier ice, the principle of the technique applies to any scattering medium. For cold media - glacier ice, sea ice and snow - there are important differences for how the effective scattering length relates to established quantities. In bubbly ice, previous work assumed that the ice is solid with the refractive index being purely the one of ice. Scattering being dominated by bubbles of some average size and distance, which govern the mean-free-path of the physical scattering process (Price and Bergström, 1997; Askebjerg and others, 1997; Ackermann and others, 2006). In reality, this scattering process is far from isotropic with an average cosine of the polar scattering angle $g = |\cos \theta| \approx 0.75$ for the case of Mie scattering on spherical bubbles. It has been shown that any scattering problem in radiative transfer can be described through an effective, isotropic scattering process (Kokhanovsky, 2004). g then provides a convenient relationship between the physical mean free path l_{mfp} and the effective scattering length l_{eff} , which describes an effective, isotropic process:

$$l_{\text{eff}} = \frac{l_{\text{mfp}}}{1-g}. \quad (5)$$

While scattering is typically dominated by bubbles instead of cracks, dust and crystal boundaries (Price and Bergström, 1997; Dacic and others, 2013), these contributions may be significant close to the surface. The advantage of measuring the effective scattering coefficient directly is that no assumptions about g or the nature of the underlying scattering processes need to be made.

EXPERIMENTAL METHODS

To measure the absorption and effective scattering coefficient of glacier ice, it is necessary to measure the fluence rate and fit the result with the diffusion theory from Eq. 4. The fluence rate describes how much energy flows through a unit area at arbitrary orientation per unit time. In our setup as shown in Figure 1 we inject a laser pulse vertically into the ice. The detector is placed in the scattering-far-field, in this specific case about 1.8m away from the laser, which is of the order of $\approx 30l_{\text{eff}}$. A realistic detector has a finite area defined by the area imaged by the collection optics. Therefore, the appropriate function to use for a fit is the fluence rate integrated over this area, which possesses units of energy per unit time. Realistically, placing such a detector in the scattering-far-field introduces many orders of magnitude of loss (Allgaier and Smith, 2021), which can only be overcome by using photon-counting detectors, a feature absent from most commercial LiDAR systems. At the same time, these detectors provide excellent temporal resolution.

While pulsed laser sources, photon counting detectors and the necessary timing electronics are all commercially available, not all varieties are affordable or appropriate. As shown in Allgaier and Smith (2021), the expected duration of the fluence rate distribution is between 100ns and 1000ns, which implies that a 10ns-duration laser pulse is significantly shorter than the overall distribution, rendering it effectively "instantaneous". The same is true for the employed electronics: The measurement can be implemented using the counter circuit of many data acquisition systems with ns-resolution. This option can offer sufficient resolution at comparatively lower cost.

We employ a nanosecond-pulsed diode laser (*Thorlabs*) set to a pulse duration of 18ns and a repetition rate of 1MHz. All measurements are repeated with three different wavelengths. 405nm is close to the absorption-minimum of ice (Warren, 2019). 520nm is close to the laser used by ATLAS onboard ICESat-2 (532nm). The third laser at 640nm serves as a reference. In transmission measurements, it has been assumed that the absorption coefficient of ice is mostly independent of LAPs at wavelengths longer than 600nm. With the laser at 640nm we can test this assumption. At a pulse duration of 18ns the laser emits reasonable pulse energies (70pJ at 405nm, 57pJ at 520nm and 95pJ at 640nm) without drastically diminishing the temporal resolution dominated by other components.

The detector is a photo-multiplier tube (PMT) module (*Hamamatsu*) with an active area 5mm in diameter. Scattered light is collected by a lens with NA=2 (25 mm diameter, focal length 50 mm) and spectrally filtered with a 10nm-bandwidth bandpass filter centered on each laser wavelength

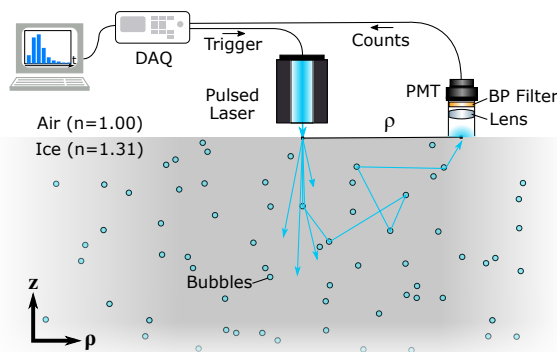


Fig. 1. The experimental setup is at core similar to a photon counting LiDAR. The light source is a diode laser module, which emits pulsed when triggered by the data acquisition module (DAQ). A delayed trigger pulse is used to gate the DAQ's counting circuit, which therefore only counts the events received from the photon counting detector in a discrete time interval after pulse emission. The arrival-time histogram is integrated in the LabView computer interface by shifting the delay between laser trigger and counter gate in constant time intervals. The backscattered light is collected onto the detector using a 50mm-focal length lens and cleaned of most background light with a 10nm-bandwidth bandpass filter. Both optical elements are inside a lens tube, which provides shielding from background. The photon counting detector is a photo-multiplier tube (PMT) with an active area 5mm in diameter.

(*Thorlabs*), both placed in lens tubes which do not require alignment in the field. The detector has a quantum efficiency of 12% at 640nm that outputs TTL pulses with a rise time of <1.5ns upon detecting a photon. The lens is set to focus collimated light onto the active area, effectively imaging an area 25mm in diameter. Even with the bandpass filter in place, the photon-counting PMT module is saturated and possibly destroyed in daylight conditions. Therefore, measurements must be conducted after sunset.

In our setup, the time-resolved measurement is implemented using a data acquisition module (DAQ - *National Instruments*). We use one counter circuit to generate a pulse train with a repetition rate of 1MHz to trigger the laser. A second counter circuit is used to generate a pulse train that is synchronized to the first one except for a time delay. This second pulse train acts as a time gate for the third circuit which is used as an even counter. When gated, the counter circuit only counts events that arrive in the time window defined by the duration of the gate pulse. In this configuration, the fluence rate $\phi(\rho, T)$ can be measured as a function of delay T from the laser pulse launch time in a time interval of 20ns, which is approximately equal to the input laser pulse duration. The measured time-of-flight (ToF) histogram is the average fluence rate in the measured time interval of

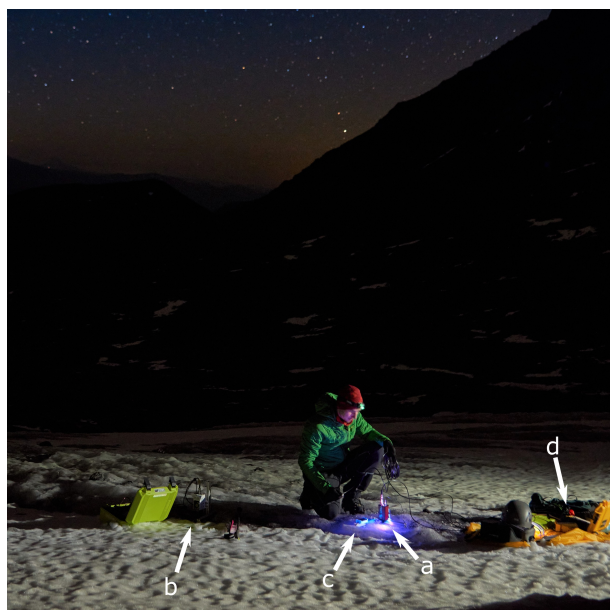


Fig. 2. Backscattered blue light can be seen right below the laser (a). The PMT is positioned to the left (b). A GPS receiver is co-located with the laser (c). The DAQ remains in its hard case (d).

20ns length, integrated over the detector area. The complete ToF histogram, is measured by stepping the delay T between the laser trigger and the counter gate pulse trains. With the temporal resolution of 20ns (limited by the gate duration) and a pulse repetition rate of 1MHz, we can resolve ToF distributions as short as a few time bins (one time bin being the gate duration of 20ns), and as long as the time between two pulses (1000ns). Since the laser is triggered externally using the DAQ, these parameters can all be easily adjusted in the field.

The histograms are evaluated with the native bin size of 20 ns as defined by the gate pulse duration of the DAQ. The last 5 bins ($t=900\dots 1000$ ns), which we can assume to only contain background, are averaged and the resulting background contribution is subtracted from all bins. Given laser-detector separation ρ (measured with a tape measure) and detector diameter d , Eq. 4 is then integrated over the interval $\rho - d/2; \rho + d/2$ and fitted to the measured ToF histogram (solid lines).

The setup does not need any alignment in the field and can be powered using a 200Wh 12V battery for the DAQ and laser and a 50Wh battery for the PMT (*Goal Zero*), which provide a runtime of roughly 10 hours on the ice, rechargeable using portable solar panels. The DAQ is controlled using a LabView interface run on a tablet computer. The combination of being battery powered, using low-power (effec-

tively class-1) lasers and transporting the instrument on foot ensures minimal environmental impact and enabled us to work in designated wilderness areas. Figure 2 shows the instrument in operation on Collier Glacier in the Three Sisters Wilderness, Oregon.

A complete list of parts required to built this setup (a cost of roughly \$10,000) and further explanation of the timing circuitry can be found in the appendix.

STUDY AREA

Field work was conducted on Collier Glacier located in the Three Sisters Wilderness, Oregon, USA (see Figure 3). Collier Glacier, is a temperate valley glacier in Oregon with an elevation of between 2300 m and 2700 m and an area of roughly 0.7km² (Mountain, 1978; Beedlow, 2011). Data was collected at two sites (44.169444°N, 121.788256°W, 2324 m and 44.167509°N, 121.784424°W, 2406 m, respectively) on September 24th and 25th during which the glacier was mostly free of snow, with only the crevasses and upper-glacier being covered by a recent layer of snow (the measurements were made on bare ice).

Data collection was performed starting about 1 hour after sunset (8:00) when the background light level had subsided sufficiently as to not saturate the PMT. At each site, 8-10 measurements at each wavelength (405, 520 and 640 nm) were taken over the course of 3-4 hours, with the initial setup taking not more than 15 minutes. For these measurements, the laser and detector were moved to different positions on an area of 4×6m, where the distance between laser and detector was kept between 1.5 m and 1.9 m, determined with a tape measure. All measurements were completed for one wavelength before moving on to the next. This order is preferable over taking three measurements at different wavelengths at the same location, because the laser head needs several minutes to warm up and achieve constant output power.

In addition to the measurements on Collier Glacier, a series of measurements aimed at determining optimal distance between the laser source and the detector was conducted on September 16th on the nearby Crook Glacier (44.079917N, 121.698415W, 2506 m), which unlike Collier Glacier widely lacks reference data from previous research but offers far easier access. On Crook Glacier, the laser mount was kept in the same position throughout the night, swapping the laser heads in place to ensure that measurements at different wavelengths were comparable. The detector was moved to distances from the laser between 0.8 m and 2.5 m with the goal of establishing a useful distance range in which ToF histograms could be measured with a reasonably well-resolved

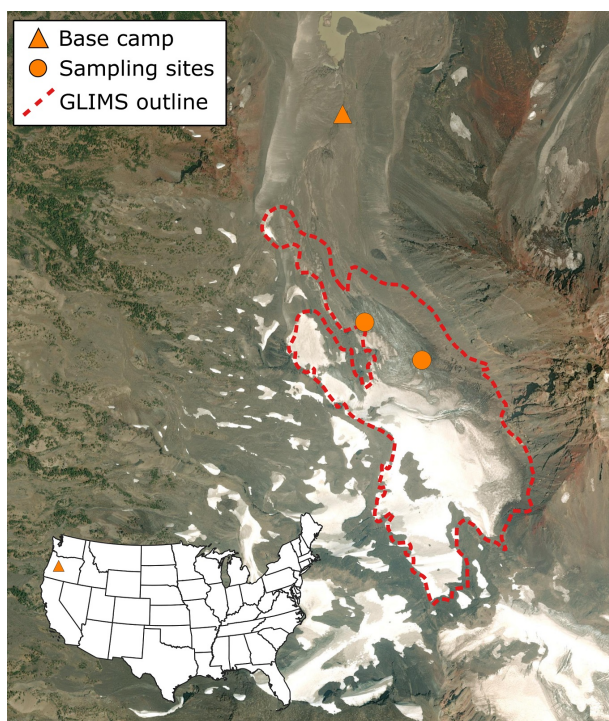


Fig. 3. The study area on Collier Glacier, Three Sisters Wilderness, Oregon. (a) Two sites were sampled: One close to the northern terminus, and one in the middle of the glacier. (b) Site 2, close to the middle of the glacier below the ice fall which roughly marks the average ELA.

peak (histogram occupying at least 5-6 bins) and sufficient signal-to-noise ratio (SNR - at least 1000 counts per bin after background-subtraction).

RESULTS

Calibration of laser-detector separation

Measurements taken on Crook Glacier indicated that the appropriate distance between laser source and detector was between 1.5 m and 2 m. Below 1.5 m, the peak of the ToF histogram was poorly resolved due to insufficient temporal bin width, especially for the red 640 nm-laser, where absorption is stronger. Above 2 m, ToF histograms were increasingly hard to measure, with the required integration time exceeding 10 minutes accompanied by poor SNR. Note that the laser mount was left in place to keep alignment constant, which is necessary to compare measurements at different wavelengths.

For the ideal separation, we show three ToF histograms recorded at a distance of 1.4 m in Figure 4. The figure also

shows that same result of the fit with the absorptive and scattering component turned off, respectively (cyan and magenta dashed lines, respectively), re-scaled for better visibility. This shows that the rising edge of the distribution is governed mostly by the scattering coefficient, and the falling edge and slow fall-off is where the absorption coefficient is extracted. With identical laser position, all three measurements yield comparable scattering coefficients ($17(\pm 4)m^{-1}$, $14(\pm 4)m^{-1}$ and $20(\pm 4)m^{-1}$, respectively for 405nm, 520nm and 640nm), where we assume a relative uncertainty of 25%, derived from the reliability of the curve fit on simulated data (Allgaier and Smith, 2021). The absorption coefficients extracted from the fitted curve ($0.16(\pm 0.04)m^{-1}$, $0.15(\pm 0.04)m^{-1}$ and $0.4(\pm 0.1)m^{-1}$, respectively for 405 nm, 520 nm and 640 nm) are in the range of literature values (Warren and Brandt, 2008).

It can, however, be seen that the peak is poorly resolved at 640nm, which can be attributed to the strong absorption at that wavelengths, resulting in a truncated peak structure, which does not change as a function of distance. We would require higher temporal resolution to resolve the peak at 640 nm. At smaller separation, the peak onset is poorly resolved at all wavelengths. At separations larger than 2 m, histograms are exceedingly hard to measure, requiring large integration times. Therefore, we conclude that the ideal distance between detector and laser source for the study area is between 1.5, and 2 m. Overall, our instrument successfully retrieved both scattering and absorption coefficients through successful curve fits, especially for 405nm and 520nm, where both the peak onset and the tail of the distributions are well resolved.

Statistical independence of scattering and absorption coefficient

One advantage of using the method presented here over stationary intensity measurements is that no assumptions about the quantity and wavelength-dependency of the measured coefficients are required (see Warren and others (2006) for a discussion of this important aspect in traditional measurement techniques). In addition, the measurement of the two coefficients is in theory fully independent, as long as the ToF histogram is sufficiently resolved (Allgaier and Smith, 2021). To test this assumption, a large and diverse data set is needed to ensure that there are no actual correlations in the underlying coefficients. It is therefore reasonable to include data from different locations and at different wavelengths, so that the range of measured coefficients and combinations thereof is as large as possible. For this purpose, we combine the data measured at both sites on Collier Glacier as well as the calibration site on Crook Glacier and use all three

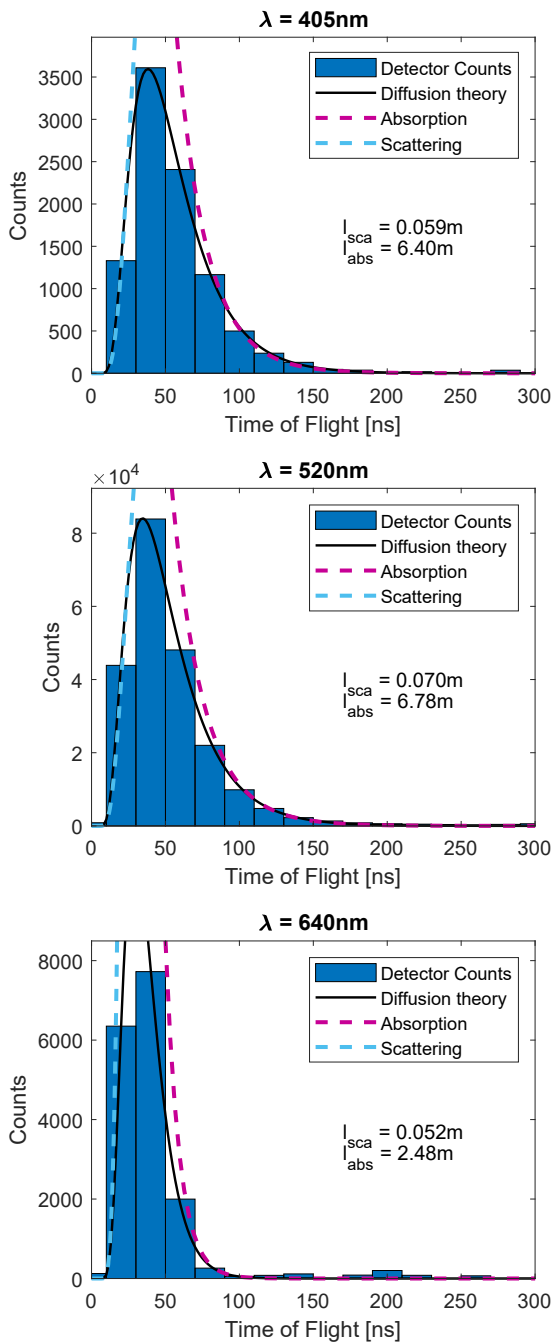


Fig. 4. Arrival-time histograms for the three different wavelength as recorded on Crook Glacier. Blue bars represent the background-subtracted data. The solid black line is the fitted diffusion curve, from which absorption and scattering coefficient are extracted. The cyan and magenta dashed lines are the diffusion curve with the absorptive and scattering component, respectively, turned off.

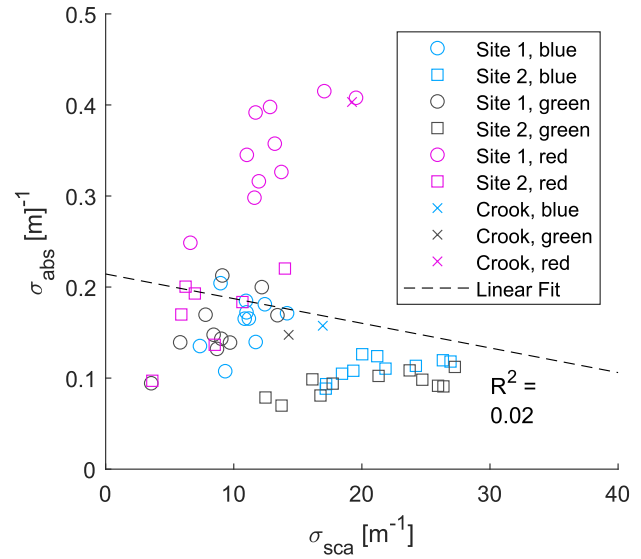


Fig. 5. All combined data points for scattering and absorption coefficients from both Crook and Collier glacier at all three wavelengths. The dashed line represents a linear fit, with the data being poorly represented by that fit ($R^2 = 0.02$), which illustrates the statistical independence of the retrieved parameters.

wavelengths. The fits for all histograms were unsupervised using identical initial parameters. For 61 out of all 65 measurements, the fits show good convergence. The remaining four show unphysically large fit uncertainties. Unsurprisingly, these are also measurements where the onset of the ToF peak is poorly resolved. A scatter plot of the successful measurements is shown in Figure 5.

To establish whether the extracted value pairs are statistically independent or not, we perform a linear fit and calculate the R^2 of the distribution, which is 0.02, demonstrating that a linear best fit represents the distribution no better than a simple average. It is clear from Figure 5 that the data set is not fully uniform and correlations within one site or wavelength exist, especially so for red light (640nm). However, overall correlations appear minor, which is the important property in this case.

Results from Collier Glacier

The extracted scattering and absorption coefficients for the two sites are shown in Figure 6. Thicker symbols represent the mean coefficient pair at each wavelength, with the error bars representing the standard deviation. First, it can be seen that the scattering coefficients for the green and blue wavelength, for which the peaks of the ToF distribution are gen-

erally well resolved, are comparable at each of the two sites. The red scattering coefficients seem to be significantly different from the others at the two sites. This is also true when we average the coefficients over both sites ($16.0(\pm 1.4)\text{m}^{-1}$, $14.9(\pm 1.6)\text{m}^{-1}$ and $10.9(\pm 1.0)\text{m}^{-1}$ at 405 nm, 520 nm and 640 nm, respectively), where the stated uncertainties are standard errors. While the values at 640nm differs significantly from the others, it is still within a 2σ uncertainty range. That said, we emphasize that the scattering coefficient measured at 640 nm suffers from poor temporal resolution, which implies that the scattering coefficient may be underestimated (compare site 2).

The extracted absorption coefficients provide a more uniform picture. Average values at 405 nm and 520 nm are almost identical and, as expected, red absorption is stronger than green and blue. The absorption coefficients (10^{-1}m^{-1}) are at the upper end of the range of previously published values (Warren and Brandt, 2008) (c.f. Figure 12 of Cooper and others (2021)), suggesting that the ice we measured at Collier Glacier contained substantial concentrations of BC or other LAPs. Such large coefficients and the fact that the absorption is almost identical for the green and blue part of the spectrum agree with observations made on icebergs and glacier ice contaminated with algae and organic LAPs (Warren and others, 2019). The fact that the absorption coefficient at Site 2 is lower than it is on Site 1 would also indicate a larger albedo, consistent with previous observations on Collier Glacier, where the broadband albedo was found to be lower at the terminus (Mountain, 1978).

While previous work often considered the absorption coefficient at wavelengths >600 nm to be independent of LAPs, it is apparent from simulations of snow albedo that this is only true for small concentrations (Warren and Wiscombe, 1980). However, due to its smaller scattering coefficient, ice albedo would depend more strongly on the absorption coefficient and LAPs. We will elaborate on this aspect in the next section for the example of BC.

To summarize, the observed absorption coefficients are consistent with glacier ice contaminated by LAPs, which is to be expected for any glacier outside of the Arctic.

Outlook: Penetration depth, Albedo and LAP concentration

Our measured scattering and absorption coefficients are relevant to a number of different applications, including inference of laser altimeter penetration depth, albedo, and LAP concentrations. Firstly, the effective scattering length represents the depth at which the direction of scattered photons has been fully randomized. In the limit of small absorption, this is the approximate depth at which a maximum

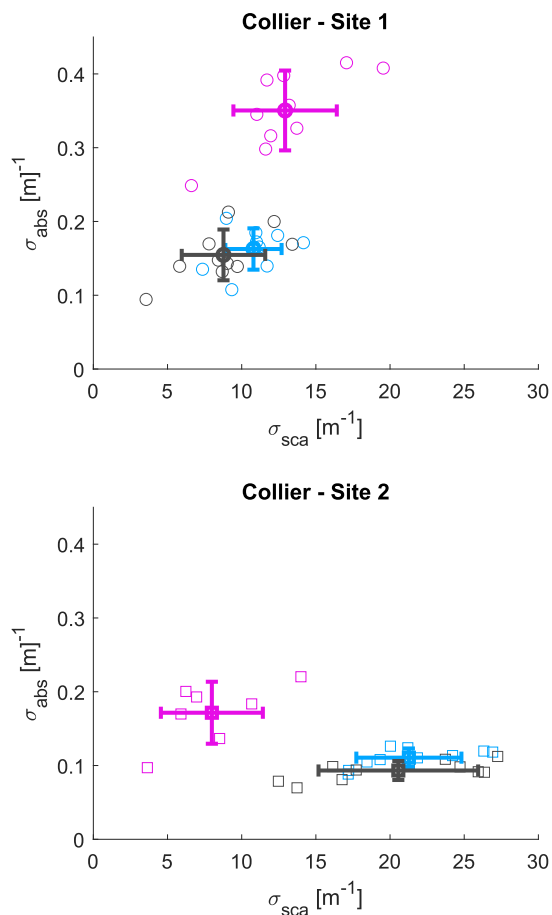


Fig. 6. Scattering and absorption coefficients from the two sites on Collier Glacier with black, cyan and magenta representing data taken at 405nm, 520nm and 640nm, respectively. Thick symbols are the mean scattering and absorption coefficient for each wavelength, and the error bars representing the standard deviation of each distribution.

of backscattering to the surface occurs. In the context of laser altimetry or LiDAR mapping, this can be interpreted as the penetration depth. Averaged over both sites, the scattering length at 520 nm (close to common wavelengths for LiDAR systems) is 6.9 cm, meaning that LiDAR measurements taken at nadir need to account for such a bias. Our measurements can be considered a first-order approximation of this bias, but more work is needed to quantify the magnitude and variability of this bias over different surfaces and to understand effects such as pulse broadening.

Secondly, it has been shown that the radiative transport for bubbly glacier ice can be framed in terms of effective bulk scattering and absorption coefficients (Dombrovsky and Kokhanovsky, 2020) like the ones measured here. To this end, we first define the effective single-scattering albedo $\omega = \sigma_{\text{eff}} / (\sigma_{\text{eff}} + \sigma_{\text{abs}})$. Since the refractive index of ice n is larger than that of air, total internal reflection occurs for upwelling radiation impinging on the air-ice-interface at angles larger than $\mu_c = \sqrt{1 - (1/n^2)}$. Dombrovsky and Kokhanovsky (2020) then define the following parameters needed to express the reflectance function:

$$\xi^2 = \frac{4}{(1 + \mu_c)^2} \frac{1 - \omega}{1 - \omega\mu_c}, \quad \chi = \frac{\omega(1 - R(1))}{1 - \omega}, \quad \gamma = \frac{1 - R(1)}{1 + R(1)}, \quad (6)$$

where $R(1)$ is the Fresnel reflection coefficient at normal incidence. The plane albedo r_p then reads

$$r_p(\mu_i) = R(\mu_i) + \frac{\gamma}{2n^2} \frac{\xi^2 \chi}{(\xi + 1/\mu_i)[\xi + 2\gamma/(1 + \mu_c)]}. \quad (7)$$

where μ_i is the cosine of the incidence angle.

Note that this equation takes into account a specular surface reflection. Using this expression we can calculate the plane albedo for any angle of incidence. By extrapolating the measured spectral components from 405-640 nm into the UV and IR by assuming that the absorption coefficient is independent of LAPs outside of the visible range (Warren and Brandt, 2008), and taking the average of the measured scattering coefficients to calculate a complete spectral albedo curve. The results for an incident angle of 60° are shown in Figure 7, where reduction in spectral albedo throughout the visible spectrum from Site 2 to Site 1 is visible. We also show the spectral albedo assuming clean ice and measured scattering coefficients. To estimate a broadband albedo at each site, we calculate a weighted average of the spectral albedo, using a solar spectrum calculated with COART (Jin and Stamnes, 1994) as a weight. Values obtained in this way are 0.47 ± 0.03 and 0.54 ± 0.03 for Site 1 and 2, respectively, and 0.62 assuming clean ice.

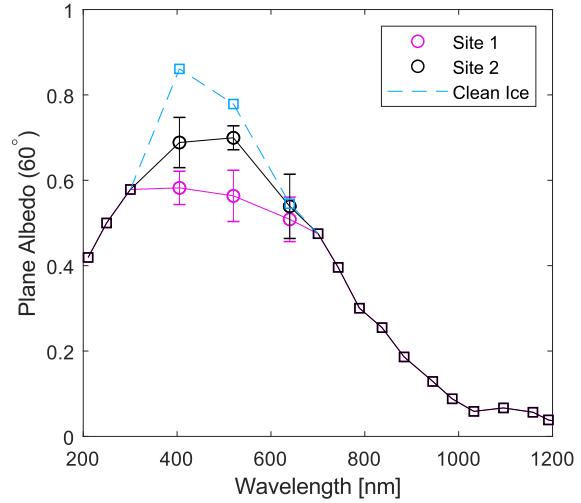


Fig. 7. Spectral albedo on both sites as well as for clean ice. Data points at 405nm, 520nm and 640nm are calculated from measured scattering and absorption coefficients (open circles). Other data points are calculated from literature values for absorption and the averaged measured scattering coefficient (open squares). Solid lines represent linear interpolation as a guide to the eye. The dashed line was calculated using absorption coefficients for clean ice and the scattering coefficients from site 2.

Although established methods from reflectance spectroscopy provide measured spectral albedos, such techniques typically only answer the question *what* the albedo is. In contrast, our method provides the underlying absorption and scattering length scales that explain *why* albedo assumes a particular value, and decouples absorption and scattering properties, thus eliminating the need for further measurements of structure or composition.

Lastly, we use the measured absorption coefficient to estimate effective concentrations of LAPs. For this, we require a baseline absorptivity for clean ice, which can be found in (Warren and others, 2006). At 405 nm, in the spectral region most sensitive to LAPs given the low native absorption coefficient of ice, we assume a value of $\sigma_{\text{clean}} = 7.78 \times 10^{-4} \text{ m}^{-1}$. The density $d = 870 \text{ kg/m}^3$ has been measured using an ice screw with a diameter of 1.3 cm and length of 15 cm as a sampler. For this demonstration, we assume that BC is the only LAP, which implies that extracted concentrations are an upper bound. We assume an Angstrom coefficient of 1.1 and a mass absorption cross section of $C_{BC} = 8.9 \text{ m}^2 \text{ g}^{-1}$ at $\lambda_{\text{ref}} = 450 \text{ nm}$ (Doherty and others, 2014). Using these values the concentration can be calculated using

$$C = \frac{\sigma_{\text{abs}} - \sigma_{\text{clean}}}{d C_{BC} (\lambda / \lambda_{\text{ref}})^{-1.1}}. \quad (8)$$

For the two sites, this yields BC concentrations of $18.6(\pm 3.2)$ ppb and $12.6(\pm 1.4)$ ppb, respectively. These values are well within the range of values previously reported for the region which lie between 6 ppb in Washington State and 156 ppb in Eastern Oregon (Doherty and others, 2014) and in summer snow on Mount Olympus, Washington State (Kaspari and others, 2015). Although future work is needed to validate this estimate from laboratory analysis of ice from Collier Glacier, the range of values obtained demonstrates the utility of the measurements and the principle of the method. That said, laboratory analysis of LAP content and debris in snow and ice also suffers from limitations, with part of the particulate mass often not accounted for in dust and BC analysis. This leads to large uncertainty in the apparent optical properties estimated from laboratory analysis, further highlighting the utility of quantifying absorption independently from scattering. Both pathways - estimating LAP content from measurement of optical properties and estimating optical properties from LAP content - ultimately rely on precise knowledge of the mixing ratio and optical properties of each LAP. With the tight grouping of measured absorption coefficients shown in Figure 6, the technique presented here could provide reasonably accurate estimates of LAP concentrations in the field. This is particularly important for diagnosing cryospheric change in remote locations, where retrieval of ice cores and physical samples is logistically difficult and costly, and therefore presents a unique opportunity to simplify data collection. It is notable that bare ice albedo appears more sensitive to LAPs than snow, an effect that has been observed for sea ice as well (Marks and King, 2013).

In summary, there are several valuable metrics that can be inferred from measured absorption and scattering coefficients. Since these measured values are effective properties of the bulk, no additional knowledge about the physical structure or assumptions about LAP content are needed, making these calculations particularly simple.

DISCUSSION

We have shown that the portable instrument presented here can resolve photon time-of-flight (ToF) histograms in temperate, near-surface glacier ice. While this process works for short visible wavelengths, improvements in temporal resolution would be desirable for red and infrared light. For most data shown here, measured ToF histograms are of sufficient quality to extract optical scattering and absorption coefficients of bare glacier ice. While measurements taken at 640 nm are at the temporal resolution limit, impairing retrieval of the scattering coefficient, improved resolution could be enabled with a time-to-digital converter or FPGA-based elec-

tronics. The current setup can be implemented for roughly \$7,000. While additional improvements such as a laser with higher pulse energy or shorter pulse duration would further reduce measurement duration and increase resolution and SNR, they would also increase cost.

The coefficients measured here are near the upper end of the range of previously reported values in the literature (Cooper and others, 2021), which implies that our setup can resolve ToF histograms on glaciers with similar composition. For clean ice characteristic of polar regions, reported absorption coefficients of near-surface ice are smaller but, along with scattering coefficients, may exhibit greater spatial variability associated with greater range of ice histories exposed at the surface. For example, differences between the scattering and absorption coefficients of deep ice melting out near the terminus of large glaciers and ice sheets relative to younger ice near the equilibrium line altitude may be explainable in terms of a common age or ice provenance. Therefore, the ToF histogram approach presented here could provide additional context for optical coefficients measured by others in Greenland (Cooper and others, 2021) and Antarctica (Ackermann and others, 2006), and could provide the basis for a systematic investigation of underlying structural controls on ice sheet albedo, which has been identified as a measurement priority needed to improve albedo parameterizations in large scale models (Dadic and others, 2013).

Direct measurements of optical properties eliminate assumptions about structure and composition of ice. The simultaneous measurement of scattering and absorption properties allows us not only to infer LAP concentrations and albedo, but also to link these surface optical properties directly to the underlying features in composition and structure. With this complex set of parameters derived from a single measurement, it becomes possible to better understand the optical properties of bare ice and build useful albedo models. In addition, albedos inferred from scattering and absorption coefficients can be interpreted in terms of structure and composition, which is not practical with albedo measurements alone. They in fact lie on the higher end of the range of previously reported absorption coefficients, which is expected for a mid-latitude glacier, where concentrations of LAPs can be expected to be higher than in the Arctic or Antarctic regions. An example is the dependence of bare ice albedo on LAP concentration illustrated here: As the scattering coefficient is lower in bare ice as compared to snow, the dependence of the albedo on the absorption coefficient is stronger, making glacier ice albedo much more susceptible to LAPs. We observe significant albedo lowering of 0.07 from a difference in BC concentration of only 6ppb. In snow, such drastic lowering of the broadband albedo would require BC

concentrations of several 1000ppb (Warren and Wiscombe, 1980). In conclusion, albedo of higher density ice with lower bubble concentration like that found in the Greenland ablation zone (Cooper and others, 2021) would be highly susceptible to even small concentrations of LAPs.

Knowledge of the optical properties of glacier ice are needed to understand LiDAR interactions with snow and ice, including penetration depth. In addition, it has been shown that precise measurement of the directional dependence of the scattering coefficient can potentially identify the average crystal C-axis orientation and therefore flow direction (Aartsen and others, 2013; Katlein and others, 2014; Rongen and others, 2020; Rongen and Chirkin, 2021). All this information can be made available in the field including rugged, remote terrain, reducing the need for sample shipping and off-site analysis, which could provide significant savings in cost and simplify expedition logistics. The non-invasive and small footprint nature of the instrument allows for deployment in remote areas such as the United States federally-designated Wilderness Areas, where motorized access and invasive measurement techniques are typically prohibited.

With more advanced techniques for photon-counting LiDAR such as photon-number threshold detection on the horizon (Cohen and others, 2019), we hope to further improve the sensitivity to the point where it becomes possible to resolve the small scattering contributions of LAPs and dust. The individual behavior of contributions such as dust has only recently been measured (Cremonesi and others, 2020), enabling us to potentially include such behavior into our model.

DATA AVAILABILITY

The raw data for all ToF histograms along with the code required to evaluate them and extract scattering and absorption coefficients are available at <https://doi.org/10.5281/zenodo.5828621>.

CODE AVAILABILITY

The code used for evaluating each ToF measurement is published alongside the raw data at <https://doi.org/10.5281/zenodo.5828621>. The LabView interface used to perform the measurement can be found at <https://doi.org/10.5281/zenodo.5828379>. An online version of the COART code used to simulate the solar spectrum used in the broadband albedo calculation is available at <https://cloudsgate2.larc.nasa.gov/jin/coart.html>.

ACKNOWLEDGEMENTS

This work was supported by the University of Oregon through the Renee James Seed Grant Initiative. We thank Nicolas Bakken-French, Kyle Strachan and Jon Meyers for their help with field work.

REFERENCES

- Aartsen M, Abbasi R, Abdou Y, Ackermann M, Adams J, Aguilar J, Ahlers M, Altmann D, Auffenberg J, Bai X, Baker M, Barwick S, Baum V, Bay R, Beatty J, Bechet S, Becker Tjus J, Becker KH, Bell M, Benabderrahmane M, BenZvi S, Berdermann J, Berghaus P, Berley D, Bernardini E, Bernhard A, Bertrand D, Besson D, Binder G, Bindig D, Bissok M, Blaufuss E, Blumenthal J, Boersma D, Bohaichuk S, Bohm C, Bose D, Böser S, Botner O, Brayeur L, Brown A, Bruijn R, Brunner J, Buitink S, Carson M, Casey J, Casier M, Chirkin D, Christy B, Clark K, Clevermann F, Cohen S, Cowen D, Cruz Silva A, Danninger M, Daughhete J, Davis J, De Clercq C, De Ridder S, Desiati P, de With M, DeYoung T, Díaz-Vélez J, Dunkman M, Eagan R, Eberhardt B, Eisch J, Ellsworth R, Euler S, Evenson P, Fadiran O, Fazely A, Fedynitch A, Feintzeig J, Feusels T, Filimonov K, Finley C, Fischer-Wasels T, Flis S, Franckowiak A, Franke R, Frantzen K, Fuchs T, Gaisser T, Gallagher J, Gerhardt L, Gladstone L, Glüsenkamp T, Goldschmidt A, Golup G, Goodman J, Góra D, Grant D, Groß A, Gurtner M, Ha C, Haj Ismail A, Hallgren A, Halzen F, Hanson K, Heereman D, Heimann P, Heinen D, Helbing K, Hellauer R, Hickford S, Hill G, Hoffman K, Hoffmann R, Homeier A, Hoshina K, Huelsnitz W, Hulth P, Hultqvist K, Hussain S, Ishihara A, Jacobi E, Jacobsen J, Japaridze G, Jero K, Jlelati O, Kaminsky B, Kappes A, Karg T, Karle A, Kelley J, Kiryluk J, Kislak F, Kläs J, Klein S, Köhne JH, Kohlen G, Kolanoski H, Köpke L, Kopper C, Kopper S, Koskinen D, Kowalski M, Krasberg M, Kroll G, Kunnen J, Kurahashi N, Kuwabara T, Labare M, Landsman H, Larson M, Lesiak-Bzdak M, Leute J, Lünemann J, Madsen J, Maruyama R, Mase K, Matis H, McNally F, Meagher K, Merck M, Mészáros P, Meures T, Miarecki S, Middell E, Milke N, Miller J, Mohrmann L, Montaruli T, Morse R, Nahnhauser R, Naumann U, Niederhausen H, Nowicki S, Nygren D, Obertacke A, Odrowski S, Olivares A, Olivo M, O'Murchadha A, Paul L, Pepper J, Pérez de los Heros C, Pfendner C, Pieloth D, Pirk N, Posselt J, Price P, Przybylski G, Rädcliff L, Rawlins K, Redl P, Resconi E, Rhode W, Ribordy M, Richman M, Riedel B, Rodrigues J, Rott C, Ruhe T, Ruzybayev B, Ryckbosch D, Saba S, Salameh T, Sander HG, Santander M, Sarkar S, Schatto K, Scheel M, Scheriau F, Schmidt T, Schmitz M, Schoenen S, Schöneberg S, Schönherr L, Schönwald A, Schukraft A, Schulte L, Schulz O, Seckel D, Seo S, Sestayo Y, Seunarine S, Sheremata C, Smith M, Soiron M, Soldin D, Spiczak G, Spiering C, Stamatikos M, Stanev T, Stasik A, Stezelberger T, Stokstad R, Stöbl A, Strahler E, Ström R, Sullivan G, Taavola H, Taboada I, Tamburro A, Ter-Antonyan S, Tilav S, Toale P, Toscano S, Usner M, van der Drift D, van Eijndhoven N, Van Overloop A, van Santen J, Vehring M, Voge M, Vraeghe M, Walck C, Waldenmaier

- T, Wallraff M, Wasserman R, Weaver C, Wellons M, Wendt C, Westerhoff S, Whitehorn N, Wiebe K, Wiebusch C, Williams D, Wissing H, Wolf M, Wood T, Xu C, Xu D, Xu X, Yanez J, Yodh G, Yoshida S, Zarzhitsky P, Ziemann J, Zierke S, Zilles A and Zoll M (2013) Measurement of south pole ice transparency with the icecube led calibration system. *Nuclear Instruments and Methods in Physics Research Section A: Accelerators, Spectrometers, Detectors and Associated Equipment*, **711**, 73–89, ISSN 0168-9002 (doi: <https://doi.org/10.1016/j.nima.2013.01.054>)
- Ackermann M, Ahrens J, Bai X, Bartelt M, Barwick SW, Bay RC, Becka T, Becker JK, Becker KH, Berghaus P, Bernardini E, Bertrand D, Boersma DJ, Böser S, Botner O, Bouchta A, Bouhali O, Burgess C, Burgess T, Castermans T, Chirkin D, Collin B, Conrad J, Cooley J, Cowen DF, Davour A, De Clercq C, de los Heros CP, Desiati P, DeYoung T, Ekström P, Feser T, Gaiser TK, Ganugapati R, Geenen H, Gerhardt L, Goldschmidt A, Groß A, Hallgren A, Halzen F, Hanson K, Hardtke DH, Harenberg T, Hauschildt T, Helbing K, Hellwig M, Herquet P, Hill GC, Hodges J, Hubert D, Hughey B, Hulth PO, Hultqvist K, Hundertmark S, Jacobsen J, Kampert KH, Karle A, Kestel M, Kohnen G, Köpke L, Kowalski M, Kuehn K, Lang R, Leich H, Leuthold M, Liubarsky I, Lundberg J, Madsen J, Marciniowski P, Matis HS, McParland CP, Messarius T, Minaeva Y, Miočinović P, Morse R, Münich K, Nahnhauser R, Nam JW, Neunhöffer T, Niessen P, Nygren DR, Olbrechts P, Pohl AC, Porrata R, Price PB, Przybylski GT, Rawlins K, Resconi E, Rhode W, Ribordy M, Richter S, Rodríguez Martino J, Sander HG, Schlenstedt S, Schneider D, Schwarz R, Silvestri A, Solarz M, Spiczak GM, Spiering C, Stamatikos M, Steele D, Steffen P, Stokstad RG, Sulanke KH, Taboada I, Tarasova O, Thollander L, Tilav S, Wagner W, Walck C, Walter M, Wang YR, Wiebusch CH, Wischniewski R, Wissing H and Woschnagg K (2006) Optical properties of deep glacial ice at the south pole. *Journal of Geophysical Research: Atmospheres*, **111**(D13) (doi: <https://doi.org/10.1029/2005JD006687>)
- Allgaier M and Smith BJ (2021) Diffuse optics for glaciology. *Opt. Express*, **29**(12), 18845–18864 (doi: [10.1364/OE.425630](https://doi.org/10.1364/OE.425630))
- Askebjør P, Barwick SW, Bergström L, Bouchta A, Cariu S, Dalberg E, Engel K, Erlandsson B, Goobar A, Gray L, Hallgren A, Halzen F, Heukenkamp H, Hulth PO, Hundertmark S, Jacobsen J, Karle A, Kandhadai V, Liubarsky I, Lowder D, Miller T, Mock P, Morse RM, Porrata R, Price PB, Richards A, Rubinstein H, Schneider E, Spiering C, Streicher O, Sun Q, Thon T, Tilav S, Wischniewski R, Walck C and Yodh GB (1997) Optical properties of deep ice at the south pole: absorption. *Appl. Opt.*, **36**(18), 4168–4180 (doi: [10.1364/AO.36.004168](https://doi.org/10.1364/AO.36.004168))
- Beedlow AC (2011) *The use of surface energy balance models as a means to quantify changes in glacier mass balance: an application to the Collier Glacier*. Master's thesis, Oregon State University, Oregon State University
- Beres ND, Lapuerta M, Cereceda-Balic F and Moosmüller H (2020) Snow surface albedo sensitivity to black carbon: Radiative transfer modelling. *Atmosphere*, **11**(10), ISSN 2073-4433 (doi: [10.3390/atmos11101077](https://doi.org/10.3390/atmos11101077))
- Bryan GH (1890) An application of the method of images to the conduction of heat. *Proceedings of the London Mathematical Society*, **s1-22**(1), 424–430 (doi: <https://doi.org/10.1112/plms/s1-22.1.424>)
- Cohen L, Matekole ES, Sher Y, Istrati D, Eisenberg HS and Dowling JP (2019) Thresholded quantum lidar: Exploiting photon-number-resolving detection. *Phys. Rev. Lett.*, **123**, 203601 (doi: [10.1103/PhysRevLett.123.203601](https://doi.org/10.1103/PhysRevLett.123.203601))
- Cooper MG, Smith LC, Rennermalm AK, Tedesco M, Muthyala R, Leidman SZ, Moustafa SE and Fayne JV (2021) Spectral attenuation coefficients from measurements of light transmission in bare ice on the greenland ice sheet. *The Cryosphere*, **15**(4), 1931–1953 (doi: [10.5194/tc-15-1931-2021](https://doi.org/10.5194/tc-15-1931-2021))
- Cremonesi L, Passerini A, Tettamanti A, Paroli B, Delmonte B, Albani S, Cavaliere F, Viganò D, Bettiga G, Sanvito T, Pullia A and Potenza MAC (2020) Multiparametric optical characterization of airborne dust with single particle extinction and scattering. *Aerosol Science and Technology*, **54**(4), 353–366 (doi: [10.1080/02786826.2019.1699896](https://doi.org/10.1080/02786826.2019.1699896))
- Dadic R, Mullen PC, Schneebeli M, Brandt RE and Warren SG (2013) Effects of bubbles, cracks, and volcanic tephra on the spectral albedo of bare ice near the transantarctic mountains: Implications for sea glaciers on snowball earth. *Journal of Geophysical Research: Earth Surface*, **118**(3), 1658–1676 (doi: <https://doi.org/10.1002/jgrf.20098>)
- Dial RJ, Ganey GQ and Skiles SM (2018) What color should glacier algae be? An ecological role for red carbon in the cryosphere. *FEMS Microbiology Ecology*, **94**(3), ISSN 0168-6496 (doi: [10.1093/femsec/fiy007](https://doi.org/10.1093/femsec/fiy007)), fiy007
- Doherty SJ, Dang C, Hegg DA, Zhang R and Warren SG (2014) Black carbon and other light-absorbing particles in snow of central north america. *Journal of Geophysical Research: Atmospheres*, **119**(22), 12,807–12,831 (doi: <https://doi.org/10.1002/2014JD022350>)
- Dombrovsky LA and Kokhanovsky AA (2020) Solar heating of ice sheets containing gas bubbles. *Journal of Quantitative Spectroscopy and Radiative Transfer*, **250**, 106991, ISSN 0022-4073 (doi: <https://doi.org/10.1016/j.jqsrt.2020.106991>)
- Dumont M, Brun E, Picard G, Michou M, Libois Q, Petit JR, Geyer M, Morin S and Josse B (2014) Contribution of light-absorbing impurities in snow to greenland's darkening since 2009. *Nature Geoscience*, **7**(7), 509–512, ISSN 1752-0908 (doi: [10.1038/ngeo2180](https://doi.org/10.1038/ngeo2180))
- Durduran T, Choe R, Baker WB and Yodh AG (2010) Diffuse optics for tissue monitoring and tomography. *Reports on Progress in Physics*, **73**(7), 076701 (doi: [10.1088/0034-4885/73/7/076701](https://doi.org/10.1088/0034-4885/73/7/076701))

- Gardner AS and Sharp MJ (2010) A review of snow and ice albedo and the development of a new physically based broadband albedo parameterization. *Journal of Geophysical Research: Earth Surface*, **115**(F1)
- Greeley AP, Neumann TA, Kurtz NT, Markus T and Martino AJ (2019) Characterizing the system impulse response function from photon-counting lidar data. *IEEE Transactions on Geoscience and Remote Sensing*, **57**(9), 6542–6551 (doi: 10.1109/TGRS.2019.2907230)
- Hadley OL and Kirchstetter TW (2012) Black-carbon reduction of snow albedo. *Nature Climate Change*, **2**(6), 437–440, ISSN 1758-6798 (doi: 10.1038/nclimate1433)
- Haskell RC, Svaasand LO, Tsay TT, Feng TC, McAdams MS and Tromberg BJ (1994) Boundary conditions for the diffusion equation in radiative transfer. *J. Opt. Soc. Am. A*, **11**(10), 2727–2741 (doi: 10.1364/JOSAA.11.002727)
- Jin Z and Stamnes K (1994) Radiative transfer in nonuniformly refracting layered media: atmosphere–ocean system. *Appl. Opt.*, **33**(3), 431–442 (doi: 10.1364/AO.33.000431)
- Kaspari S, McKenzie Skiles S, Delaney I, Dixon D and Painter TH (2015) Accelerated glacier melt on snow dome, mount olympus, washington, usa, due to deposition of black carbon and mineral dust from wildfire. *Journal of Geophysical Research: Atmospheres*, **120**(7), 2793–2807 (doi: <https://doi.org/10.1002/2014JD022676>)
- Katlein C, Nicolaus M and Petrich C (2014) The anisotropic scattering coefficient of sea ice. *Journal of Geophysical Research: Oceans*, **119**(2), 842–855 (doi: <https://doi.org/10.1002/2013JC009502>)
- Kokhanovsky A (2004) *Light Scattering Media Optics*. Environmental Sciences, Springer, ISBN 9783540211846
- Kokhanovsky AA and Zege EP (2004) Scattering optics of snow. *Appl. Opt.*, **43**(7), 1589–1602 (doi: 10.1364/AO.43.001589)
- Libois Q, Picard G, France JL, Arnaud L, Dumont M, Carmagnola CM and King MD (2013) Influence of grain shape on light penetration in snow. *The Cryosphere*, **7**(6), 1803–1818 (doi: 10.5194/tc-7-1803-2013)
- Marks AA and King MD (2013) The effects of additional black carbon on the albedo of arctic sea ice: variation with sea ice type and snow cover. *The Cryosphere*, **7**(4), 1193–1204 (doi: 10.5194/tc-7-1193-2013)
- Meredith M, Sommerkorn M, Cassotta S, Derksen C, Ekaykin A, Hollowed A, Kofinas G, Mackintosh A, Melbourne-Thomas J, Muelbert M, Ottersen G, Pritchard H and AG S (2019) *Chapter 3: Polar Regions. IPCC Special Report on the Ocean and Cryosphere in a Changing Climate*
- Mountain KR (1978) *The Chronology, Geomorphology, and Climate of Collier Glacier with Special Reference to the Ablation Process*. Master's thesis, University of Oregon, University of Oregon
- Perovich DK and Govoni JW (1991) Absorption coefficients of ice from 250 to 400 nm. *GEOPHYSICAL RESEARCH LETTERS*, **18**(7), 1233–1235
- Perron C, Katlein C, Lambert-Girard S, Leymarie E, Guinard LP, Marquet P and Babin M (2021) Development of a diffuse reflectance probe for in situ measurement of inherent optical properties in sea ice. *The Cryosphere*, **15**(9), 4483–4500 (doi: 10.5194/tc-15-4483-2021)
- Price PB and Bergström L (1997) Optical properties of deep ice at the south pole: scattering. *Appl. Opt.*, **36**(18), 4181–4194 (doi: 10.1364/AO.36.004181)
- Rongen M and Chirkin D (2021) A novel microstructure-based model to explain the icecube ice anisotropy
- Rongen M, Bay RC and Blot S (2020) Observation of an optical anisotropy in the deep glacial ice at the geographic south pole using a laser dust logger. *The Cryosphere*, **14**(8), 2537–2543 (doi: 10.5194/tc-14-2537-2020)
- Ryan JC, Hubbard A, Stibal M, Irvine-Fynn TD, Cook J, Smith LC, Cameron K and Box J (2018) Dark zone of the greenland ice sheet controlled by distributed biologically-active impurities. *Nature communications*, **9**(1), 1–10
- Saito M, Yang P, Loeb NG and Kato S (2019) A novel parameterization of snow albedo based on a two-layer snow model with a mixture of grain habits. *Journal of the Atmospheric Sciences*, **76**(5), 1419 – 1436 (doi: 10.1175/JAS-D-18-0308.1)
- Skiles SM, Flanner M, Cook JM, Dumont M and Painter TH (2018) Radiative forcing by light-absorbing particles in snow. *Nature Climate Change*, **8**(11), 964–971, ISSN 1758-6798 (doi: 10.1038/s41558-018-0296-5)
- Smith BE, Gardner A, Schneider A and Flanner M (2018) Modeling biases in laser-altimetry measurements caused by scattering of green light in snow. *Remote Sensing of Environment*, **215**, 398–410, ISSN 0034-4257 (doi: <https://doi.org/10.1016/j.rse.2018.06.012>)
- Trodahl HJ, Buckley RG and Brown S (1987) Diffusive transport of light in sea ice. *Appl. Opt.*, **26**(15), 3005–3011 (doi: 10.1364/AO.26.003005)
- Warren SG (2019) Optical properties of ice and snow. *Philosophical Transactions of the Royal Society A: Mathematical, Physical and Engineering Sciences*, **377**(2146), 20180161 (doi: 10.1098/rsta.2018.016)
- Warren SG and Brandt RE (2008) Optical constants of ice from the ultraviolet to the microwave: A revised compilation. *Journal of Geophysical Research: Atmospheres*, **113**(D14) (doi: <https://doi.org/10.1029/2007JD009744>)

- Warren SG and Wiscombe WJ (1980) A model for the spectral albedo of snow. ii: Snow containing atmospheric aerosols. *Journal of Atmospheric Sciences*, **37**(12), 2734 – 2745 (doi: 10.1175/1520-0469(1980)037<2734:AMFTSA>2.0.CO;2)
- Warren SG, Brandt RE and Grenfell TC (2006) Visible and near-ultraviolet absorption spectrum of ice from transmission of solar radiation into snow. *Appl. Opt.*, **45**(21), 5320–5334 (doi: 10.1364/AO.45.005320)
- Warren SG, Roesler CS, Brandt RE and Curran M (2019) Green icebergs revisited. *Journal of Geophysical Research: Oceans*, **124**(2), 925–938 (doi: <https://doi.org/10.1029/2018JC014479>)
- Williamson CJ, Anesio AM, Cook J, Tedstone A, Poniecka E, Holland A, Fagan D, Tranter M and Yallop ML (2018) Ice algal bloom development on the surface of the Greenland Ice Sheet. *FEMS Microbiology Ecology*, **94**(3), ISSN 0168-6496 (doi: 10.1093/femsec/fiy025), fiy025
- Wiscombe WJ and Warren SG (1980) A model for the spectral albedo of snow. i: Pure snow. *Journal of Atmospheric Sciences*, **37**(12), 2712 – 2733 (doi: 10.1175/1520-0469(1980)037<2712:AMFTSA>2.0.CO;2)
- Zhang Y, Kang S, Cong Z, Schmale J, Sprenger M, Li C, Yang W, Gao T, Sillanpää M, Li X, Liu Y, Chen P and Zhang X (2017) Light-absorbing impurities enhance glacier albedo reduction in the southeastern tibetan plateau. *Journal of Geophysical Research: Atmospheres*, **122**(13), 6915–6933 (doi: <https://doi.org/10.1002/2016JD026397>)

LIST OF PARTS

Lasers Thorlabs NPL41B, NPL52B, NPL64B

Detector Hamamatsu H7421-50 (most photon-counting PMTs can be used for this purpose)

Optical elements 50mm focal length, 25mm diameter lens, anti-reflection coated for visible light: Thorlabs LA1131-A
10nm-bandpass filters: Thorlabs FB405-10, FB520-10, FB640-10
Lens tubes: Thorlabs SM1L10

Data Acquisition National Instruments USB-6361 with BNC breakout block (any NI USB-63xx series DAQ has the same counter functions necessary to run the LabView code).

Cables RG58 cables with BNC connectors
3dB attenuator for laser triggering

GPS Receiver Garmin GLO 2

TIME-OF-FLIGHT MEASUREMENTS USING NI DATA ACQUISITION MODULES

The NI DAQs have so-called "counters", which can either count edges of TTL (5V square) pulses on a specified input or act as pulse generators. To facilitate a time-of-flight measurements, we use three counters. *Counter 0* generates a pulse train of predefined repetition rate and is supplied to an output, which is connected to the trigger input of the laser. Internally, the frequency output from *Counter 0* is routed to the trigger input of *Counter 1*, which also generates a pulse output, synchronized to *Counter 0*. The output pulse length of the output of *Counter 1* is equal to the desired gate length (time bin size). An artificial delay is applied between the trigger input from *Counter 0* and the pulse output from *Counter 1* which corresponds to the start time of the current time bin. The third counter, *Counter 2*, works as an edge counter for the pulses coming from the photon-counting detector. The pulse train from *Counter 1* is internally routed to the gate input on *Counter 2*. To record the entire ToF histogram, the delay on the pulse output of *Counter 1* needs to be step-wise increased.

Alternatively, if the laser can operate as a stand-alone pulsed source without external input, it can be used as a frequency master for the whole system. The laser needs an output, which provides a trigger signal whenever the laser fires. This trigger is then routed to an input on the DAQ. This input is then used to trigger a pulse train on *Counter 0*, with a pulse duration equal to the desired gate length (time bin size). The Frequency output from *Counter 0* is internally routed to the *Gate Input* on *Counter 1*, the TTL signal from the photon counting detector is routed to the input of *Counter 1*. The artificial delay between the trigger input and the output of *Counter 0* corresponds to the start time of the current time bin and needs to be increased step-wise to build a complete ToF histogram. With the lasers used here, this solution would work for repetition rates of 1MHz or faster, which the laser can produce without external trigger. In this configuration, a cheaper data acquisition module with only 2 counter circuits would suffice, but the setup would sacrifice the flexibility to use slower repetition rates which are required to record long ToF distributions as they would manifest for high-density, clean ice. This use of the DAQ is similar, but not identical to the "pulse separation" measurement described in the manual, which imposes further constraints on photon detection rates.

In both counter configurations, the repetition rate should be chosen so that the entire ToF distribution is captured and the measured intensity falls to the background count rate by the end of each cycle. The temporal bin size Δt can be

chosen as small as two cycles of the counter circuit's clock frequency ν_{clock} :

$$\Delta t = 2/\nu_{\text{clock}}. \quad (9)$$

In general, there are internal electronic delays between the different counter circuits, between laser trigger and optical output, as well as physical delays due to the length of cables. All of these need to be measured and subtracted from the measured ToF distribution to extract the "actual" time of flight. This is done by placing laser and detector close together and less than 30cm away from a solid surface (scattering card or a wall) and measuring a ToF histogram. The actual time of flight would be the physical path from the laser to the surface plus the distance from the surface to the detector, in this case $<2\text{ns}$, unresolvable by the system. The peak at the measured distribution indicates the internal delay, which can then be subtracted from all measured ToF distributions. With the cables used here, the internal delay is 130ns for all measurements taken on Collier Glacier and 190ns for the calibration measurements taken on Crook Glacier.

APPROXIMATE DETERMINATION OF THE SCATTERING-FAR-FIELD "BY EYE"

As a first approximation, the optical distance between source and detector can be determined "by eye", as the intensity falls off as a function of distance from the laser:

$$\phi(\rho) \propto \exp\left(-\sqrt{3\rho^2\sigma_{\text{eff}}\sigma_{\text{abs}}}\right). \quad (10)$$

In ice, this exponential fall-off is dominated by the scattering coefficient, which is much larger than the absorption coefficient. A reduction in intensity of one order of magnitude corresponds to a distance of about 3 scattering lengths. As a simple approximation, the detector should be placed outside the area of visible backscattered light, ensuring several orders of magnitude in intensity reduction. However, if this distance is too large, there will be little backscattered light, reducing SNR. For small distances, arrival times will also be shorter according to Eq. 4, meaning that temporal resolution may not be sufficient to resolve the arrival time distribution appropriately.